Chorley, H., Levy, R., Naish, T., Lewis, A., Cox, S., Hemming, S., Ohneiser, C., Gorman, A., Harper, M., Homes, A., Hopkins, J., Prebble, J., Verret, M., Dickinson, W., Florindo, F., Golledge, N., Halberstadt, A.R., Kowalewski, D., McKay, R., Meyers, S., Anderson, J., Dagg, B., and Lurcock, P., 2022, East Antarctic Ice Sheet variability during the middle Miocene Climate Transition captured in drill cores from the Friis Hills, Transantarctic Mountains: GSA Bulletin, https://doi.org/10.1130/B36531.1.

Supplemental Material

Text. Methods

Table S1. FHDP Sample List

Table S2. Palynology Counts

Table S3. Tephra Classification Data

Figure S1. Siliceous algae counts for cores FHDP-1A and -1B.

Figure S2. Siliceous algae counts for core FHDP-2A.

Figure S3. Siliceous algae counts for core FHDP-3A.

Figure S4. Downcore variability in prevalent plant genera for cores FHDP-1A, -2A, and -3A.

Figure S5. Downcore NRM magnetisation, MAD and ChRM inclination for core FHDP-1A, -2A, and -3A. The geocentric axial dipole (GAD) field inclination.

Figure S6. (A) Hysteresis and IRM. (B) data from five selected samples which shows that low-coercivity magnetic minerals are dominant. (C) and (D) First-Order Reversal Curve analyses which indicate mixtures of single-domain – multi-domain (C) and superparamagnetic – single-domain grains (D) low coercivity minerals are dominant magnetic mineral.

Figure S7. Demagnetisation behavior of Friis Hills core samples from selected intervals. (A) and (B) are reversed and normal polarity samples with relatively low noise level and a weak normal polarity viscous overprint. (C) and (D) are two reverse polarity samples with stronger normal polarity viscous overprints which we suggest resulted from rotary drilling of cores in the field. (E) an anomalously magnetised sample with a well-behaved, shallow inclination magnetisation which does not demagnetise completely at 100 mT. Such magnetisations most likely result from a strongly magnetised basement clast in the sample. (F) a weakly magnetised sample which does not demagnetise.

METHODS

Seismic refraction surveying and modeling

Three seismic transects totaling 3.72 km in length were acquired across the Friis Hills Basin in December 2014 (Figs. 2, 3) using a hand deployed 48-channel Geometrics Geode system, with a geophone interval of 5 m and a hammer source interval of 10 m. Geophone and shot locations were positioned using GNSS with elevations further constrained by a LIDAR derived local digital elevation model. The GLOBE Claritas (Ravens, 2001) refraction statics module was then used to construct simple two-layer velocity models for each line with velocities that vary laterally. The models consists of a 10–60 m thick upper layer (Fig. 3) with velocities characteristic of partially ice saturated sediments (2730–3720 m/s) overlying basement rocks with velocities consistent with granite or diorite (3450–5050 m/s).

Drilling

Three sites, (Fig. 2), were drilled to a maximum depth of 50.48 m (FHDP-3A) during the austral summer season of 2016/17, using a bespoke air chilled and flushed wire-line diamond drill system. Drill sites were located based on previous mapping (Lewis and Ashworth 2015; summarized in Fig. 2), and the seismic refraction survey. Drilling objectives were to sample the deepest part of the basin and recover continuous sections through the Friis Hill II drifts (Figs. 2, 3).

Sites were numbered FHDP 1, 2, and 3, with the suffixes A, B, and C used where more than one hole was drilled at a site. A total of 73.26 m of permafrost (ice-cemented) sediment was recovered, with an average recovery rate of 71.9%. Core 2A had the highest recovery at 75.9%, with cores 1A and 3A both recovering 70.2%. Site 1 was located to recover core from what was initially inferred to be the thickest part of the basin based on seismic refraction data. However, basement was intersected at 33.5m. Site 2 was selected to core into known outcrop of Friis II drift lower, to ensure recovery of this fossil-rich sequence. Site 3 was located near the intersection of seismic lines 2 and 3 to enhance stratigraphic correlation between each site and attempt to recover Friis I drift and intersect basement, which was not reached, and this hole was terminated due to technical difficulties. Core was unable to be recovered between 7.3–15.1 m at FHDP 1A and from the surface down to 15.02 m in FHDP 3A, due to a lack of ice cement. For these intervals, cuttings were sampled every 50 cm.

Core description and sampling

Initial visual lithological descriptions were undertaken in the field, with descriptions cross-checked and, in some cases, subsequently modified following re-description of the core prior to sampling at the National Ice Core Facility at GNS Science. Lithological descriptions for fine-grained and poorly-sorted terrigenous sediments were based on definitions established for the Cape Roberts Project and ANDRILL Programme (Hambrey et al., 1997, Naish et al., 2008, McKay et al., 2009) and terrestrial glacial environments (Walker and James, 1992, Benn and Evans, 2010, van der Meer and Menzies, 2011). A preliminary lithofacies scheme was defined based on the identification of lithology, sedimentary structure and texture, clast abundance, composition and density, deformation features, fossil content, color, and nature of contact with

underlying beds. A total of 168 samples were taken from the cores, at regular one meter intervals through diamictons and at higher resolution through the thinner and more variable lacustrine and fluvial deposits. Each sample was divided into subsamples for analysis of, grainsize, diatoms and pollen.

Grainsize analyses and clast counts

Grain size was measured on an Aqueous Liquid Module of the Beckman-Coulter LS 13 320 Laser Diffraction Particle Size Analyzer to provide quantitative data to support visual core descriptions. An ~5 cm^3 sub-sample was crushed using wooden blocks to remove aggregates produced during the drying process, and then passed through a 2 mm sieve and split into 3 subsamples of ~0.1–1 g depending on lithology. All samples were treated with 27% hydrogen peroxide at 70 °C to remove organic material and samples were examined under a microscope to check for carbonate and biogenic silica. All samples were then disaggregated by adding 50 ml of 1 g/L calgon and leaving in an ultrasonic bath for 30 min. One in ten samples were re-measured to check the reproducibility of the results and consistency of process. Gravel (>2mm) clasts exposed on the core surface were counted and summed every 10 cm interval along the core to quantify gravel content. These data can provide a measure of glacial proximity (e.g., Fielding et al., 2000; Naish et al., 2001).

Core physical and chemical properties measurements

Along-core elemental abundances were measured using a handheld M-series Vanta Olympus portable X-Ray Fluorescence (XRF) spectrometer (50 KV) at the National Ice Core Research Laboratory. Samples were calibrated using international standards from the USGS and Geological Survey of Japan and raw data were corrected using the international XRF calibration standard. High-resolution three-dimensional images of the cores were collected at Pacific Radiology, Boulcott Hospital, Lower Hutt using X-ray computed tomography (CT) conducted on a GE BrightSpeed medical CT scanner set to 120 kV, 250 mA, pitch of 0.625 mm and a 100 cm^2 window. These data were used for detailed examination of sedimentary structures, textures, deformation features and lithologies.

Diatoms

A subset of 86 samples, to include at least one from each sedimentary facies, were examined for diatom content. 50 samples from fluvial-lacustrine facies were analyzed in detail. Samples were immersed in hydrogen peroxide to remove organic matter. Biogenic silica was concentrated by flotation in Sodium Polytungstate (specific gravity 2.20 g cm^2). Material separates were rinsed and mounted on permanent slides for light microscopy (LM) using Naphrax® mountant (refractive index 1.65). Assemblage composition for each sample was determined by counting diatoms under a Leitz Diaplan differential interference contrast microscope at ×400 magnification. At least 90 (usually 200) whole and significant fragments of diatom valves (including ends or centers of valves) were identified to genus level in each sample. Only a small proportion of diatoms showed a clear affinity with extant species during initial identification. To avoid informal new forms, where possible, identification was therefore based on recognized genera.

Palynology

Nineteen samples were collected from mudstone and sandstone intervals for palynological study. These samples were processed at GNS Science using standard palynological methods: 10% cold HCl wash, 50% HF, a further 10% HCl, a brief 20–60 second disaggregation in an ultrasonic bath, followed by filter through a 6µm mesh. A single *Lycopodium* tablet (batch 1031) was added to each sample at the start of processing, to enable calculation of absolute palynomorph abundance. Organic residues were mounted on two cm square glass cover slips in glycerin jelly. A complete scan of the cover slip was made for each sample using a Zeiss Axioplan2 light microscope.

Tephra Characterization and Numeric Dating

Tephra deposits in the cores were identified during visual core description and McMurdo Volcanic Group origin was confirmed via preliminary XRF analysis of the cores, which identified intervals of relatively high Niobium (Roser and Pyne, 1989). Two tephra deposits were found at 5.6 m in cores 2A/2C (Fig. 6) and 27 m in core 3A (Fig. 7). The tephra horizon in core 2C comprised a yellow/light gray, mm-scale, cross-bedded fine sandstone with volcaniclastic material and dispersed clasts, while the horizon in 3A was a gray/brown massive mudstone with volcaniclastic grains and dispersed clast and pebble lenses.

Glass shards from each tephra horizon were extracted and analyzed for their major element composition at Victoria University of Wellington on a JEOL JXA 8230 Superprobe (EMPA), for chemical characterization, including population homogeneity. A beam size of 10 µm at 8 nA was used to analyze major elements as oxides, whose concentrations were calculated using the ZAF correction method. Matrix matched standards VG-568 and VG-A99 were used as bracketing standards and run three times between every sample, with VG-568 used as the normalization standard and VG-A99 run as the secondary standard. Accuracy of the analyses was within ≤4.6% of the recommended values for the VG-A99 except for TiO2 (13.6%), MnO (30.1%) and Cl (11.5%), precision for all the elements was ≤0.76 (2sd). Analytical totals were between 93–100 wt% with the deviations from 100% attributed to variable degrees of post eruption hydration, these deviations were corrected to 100% and are reported in the supplementary information.

Two samples were prepared for radiometric dating. Each sample was disaggregated in water and wet-sieved at 63 µm. After disaggregation and dry sieving at 150µm, feldspars were concentrated with heavy liquids, to isolate the 2.55–2.65 g/cc, and hand-picked under a binocular microscope for clarity and absence of visible inclusions. Samples were co-irradiated with Fish Canyon sanidine monitor standard in two separate batches (irradiations USGS78 and USGS90), each with an 8 h duration, with Cd-shielding and rotation in the USGS TRIGA Reactor. The second batch was irradiated because of the inadequate precision for distinguishing the ages of the two samples in the first. An analytical delay required us to omit the use of the ^{37}Ar for nuclear interference corrections on the second batch, so we used a fixed K/Ca with a large uncertainty. The magnitude of this correction is small for sanidine, allowing us to retain good age precision using this approach. To further minimize the impact of the nuclear interference corrections and to filter out measurements with large uncertainties, we filtered the analyses to exclude samples with <80% radiogenic ^{40}Ar before plotting.

Irradiated samples from irradiation USGS90 were analyzed using the fully automated LDEO-AGES Isotopx NGX multiple collector mass spectrometer. Individual crystals were fused using a Teledyne 70 Watt CO_2 laser at 15% power and gases released from the heating of samples were scrubbed of reactive gases by exposure to Zr-Al sintered metal alloy getters. Isotopic ratios were determined using Pychron, an open source software package led by developer Jake Ross (New Mexico Tech). Measurements were made in multiple-collector mode with ^{40}Ar, ^{39}Ar, ^{38}Ar, and ^{37}Ar on faraday detectors outfitted with ATONA amplifiers (Cox et al., 2020 in review), and ^{36}Ar in ion counting mode on a secondary electron multiplier. At these conditions, the ^{40}Ar signal was ~455 mV for 8.5×10^{-13} moles of atmospheric Ar.

In all cases, $^{40}Ar/^{39}Ar$ data were corrected for backgrounds, mass discrimination and nuclear interferences (except for the NGX analyses we did not make a correction for Ca interference because it was more than a year between irradiation and analysis). Background and mass discrimination corrections were based on time series of blanks and air pipettes (respectively) run throughout the interval of the analyses (Lee et al., 2006). The nuclear interference corrections were based on production ratios from (Dalrymple et al., 1981). Individual dates are reported with ± 1σ analytical uncertainties relative to Fish Canyon monitor age of 28.201 (Kuiper et al., 2008) and using the decay constants of (Min et al., 2000). J-values were calculated from Fish Canyon sanidine monitor co-irradiated in the same irradiation pit as the unknowns and other monitor standards.

Paleomagnetic Stratigraphy

A total of 72 discrete samples (48 from 3A, 14 from 2A, 10 from 1A), ranging in volume between 4 and 8 $cm^{3,}$ were cut from frozen core sections for paleomagnetic analysis. Samples were oriented only with respect to the up direction because cores are not azimuthally oriented. In polar regions the geomagnetic field has a steep inclination, which was 83° at the drill sites (77°S), enabling identification of polarity in the absence of declination. Fine-grained intervals were targeted for sampling and regions around clasts in diamicton-dominated lithofacies were avoided due to the potential for post and syn-depositional realignment of the magnetic fabric.

Frozen samples were transported to the Otago Paleomagnetic Research Facility, where they were stored in a sample freezer at −25 °C. Magnetic moment measurements were made using the 2G Enterprises DC 760–3.5 pass-through superconducting rock magnetometer housed in a 150 nT magnetically shielded laboratory at the OPRF. All samples were demagnetised in an alternating field increasing in 5 mT increments to 50 mT and then at 60 mT, 70 mT, 80 mT and 100 mT. Isothermal Remanence Magnetisation (IRM), hysteresis, loops and First-Order Reversal Curve (FORC) (Roberts et al., 2014) analyses were performed to characterize the remanence-carrying mineralogy on c. 0.10 g crushed samples using a Princeton Measurements Corporation Vibrating Sample Magnetometer (VSM, MicroMag 3900). FORCs were measured with a field spacing of 2 mT, an interaction field (H_u) ranging between −60 mT to +60 mT, and coercivity field (H_c) between 0 mT to 100 mT. The FORCinel software package (Harrison and Feinberg, 2008) was used to process data and smoothing factors of between 3 and 5 (Roberts et al., 2000) were used. Orthogonal component vector plots of the paleomagnetic data were produced, and palaeomagnetic directions calculated by principal component analysis (PCA) (Kirschvink, 1980), using the PuffinPlot software package (Lurcock and Wilson, 2012).

REFERENCES CITED

Benn, D., and Evans, D., 2010, Glaciers and glaciation: London, Hodder Education.

Cox, S., Hemming, S., and Tootell, D., 2020, The Isotopx NGX and the ATONA Faraday Amplifiers: Geochronology, https://doi.org/10.5194/gchron-2-231-2020.

Dalrymple, G., Lanphere, M., and Kraker, G., 1981, Irradiation of samples for $^{40}Ar/^{39}Ar$ dating using the Geological Survey TRIGA reactor.

Fielding, C.F., Naish, T.R., Woolfe, K.J., and Levelle, M.A., 2000, Facies analysis and sequence stratigraphy of CRP-2/2A, Victoria Land Basin, Antarctica: Terra Antarctica, v. 7, p. 323–338.

Hambrey, M., Krissek, L., Powell, R., Barrett, P., Camerlenghi, A., Claps, M., Ehrmann, W., Fielding, C., and Howe, J., 1997, Cape Roberts Project Core Logging Manual: Coring for Antarctic Tectonic and Climatic History: Antarctic Research Centre, Victoria University of Wellington.

Harrison, R., and Feinberg, J., 2008, FORCinel: An improved algorithm for calculating first-order reversal curve distributions using locally weighted regression smoothing: Geochemistry Geophysics Geosystems, https://doi.org/10.1029/2008GC001987.

Kirschvink, J., 1980, The least-squares line and plane and the analysis of palaeomagnetic data: Geophysical Journal International, v. 62, p. 699–718, https://doi.org/10.1111/j.1365-246X.1980.tb02601.x.

Kuiper, K., Deino, A., Hilgen, F., Krijgsman, W., Renne, P., and Wijbrans, J., 2008, Synchronizing Rock Clocks of Earth History: Science, v. 320, p. 500–504, https://doi.org/10.1126/science.1154339.

Lee, J., Marti, K., Severinghaus, J., Kawamura, K., Yoo, H., Lee, J.B., and Kim, J., 2006, A redetermination of the isotopic abundances of atmospheric Ar: Geochimica et Cosmochimica Acta, v. 70, p. 4507–4512, https://doi.org/10.1016/j.gca.2006.06.1563.

Lewis, A.R., and Ashworth, A.C., 2015, An early to middle Miocene record of ice-sheet and landscape evolution from the Friis Hills, Antarctica: Geological Society of America Bulletin, https://doi.org/10.1130/B31319.1.

Lurcock, P., and Wilson, G., 2012, PuffinPlot: A versatile, user-friendly program for paleomagnetic analysis: Geochemistry Geophysics Geosystems, https://doi.org/10.1029/2012GC004098.

McKay, R., Browne, G., Carter, L., Cowan, E., Dunbar, G., Krissek, L., Naish, T., Powell, R., Reed, J., Talarico, F., and Wilch, T., 2009, The stratigraphic signature of the late Cenozoic Antarctic Ice Sheets in the Ross Embayment: Geological Society of America Bulletin, v. 121, p. 1537–1561, https://doi.org/10.1130/B26540.1.

Min, K., Mundil, R., Renne, P., and Ludwig, K., 2000, A test for systematic errors in $^{40}Ar/^{39}Ar$ geochronology through comparison with U/Pb analysis of a 1.1Ga rhyolite: Geochimica et Cosmochimica Acta, v. 64, p. 73–98, https://doi.org/10.1016/S0016-7037(99)00204-5.

Naish, T., Barrett, P., Dunbar, G., Woolfe, K., Dunn, A., Henrys, S., Claps, M., Powell, R., and Fielding, C., 2001, Sedimentary Cyclicity in CRP Drillcore, Victoria Land Basin, Antarctica: Terra Antarctica, v. 8, no. 3, p. 225–244.

Naish, T., Wilson, G., Dunbar, G., and Barrett, P., 2008, Constraining the amplitude of Late Oligocene bathymetric changes in western Ross Sea during orbitally-induced oscillations in the East Antarctic Ice Sheet: (2) Implications for global sea-level changes: Palaeogeography,

Palaeoclimatology, Palaeoecology, v. 260, p. 66–76, https://doi.org/10.1016/j.palaeo.2007.08.021.
Ravens, J., 2001, Globe Claritas, Seismic Processing Software Manual: Lower Hutt, GNS Science.
Roberts, A., Heslop, D., Zhao, X., and Pike, C., 2014, Understanding fine magnetic particle systems through use of first-order reversal curve (FORC) diagrams: Reviews of Geophysics, v. 52, no. 4, p. 557–602, https://doi.org/10.1002/2014RG000462.
Roberts, A., Pike, C., and Verosub, K., 2000, First-order reversal curve diagrams: A new tool for characterizing the magnetic properties of natural samples: Journal of Geophysical Research, v. 105, p. 28,461–28,475, https://doi.org/10.1029/2000JB900326.
Roser, B., and Pyne, A., 1989, Wholerock geochemistry: Wellington, New Zealand, DSIR Publishing.
van der Meer, J., and Menzies, J., 2011, The micromorphology of unconsolidated sediments: Sedimentary Geology, v. 238, p. 213–232, https://doi.org/10.1016/j.sedgeo.2011.04.013.
Walker, R., and James, N., 1992, Facies Models: Response to Sea Level Change: Geological Association of Canada.

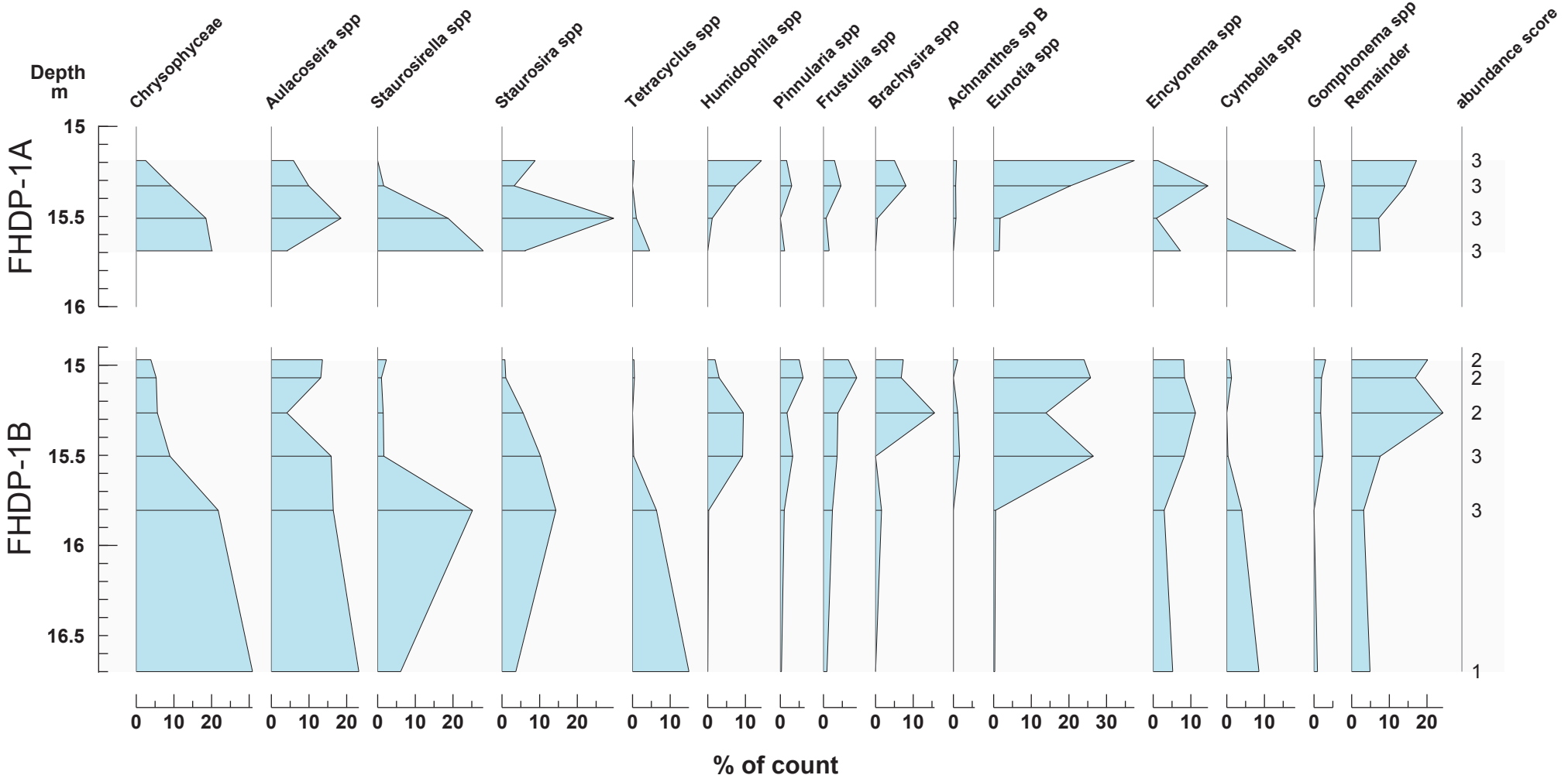
Depth
m
Chrysophyceae
Aulacoseira spp
Staurosirella spp
Staurosira spp
Tetracyclus spp
Humidophila spp
Pinnularia spp
Frustulia spp
Brachysira spp
Achnanthes sp B
Eunotia spp
Encyonema spp
Cymbella spp
Gomphonema spp
Remainder
abundance score
FHDP-1A
15
15.5
16
3
3
3
3
FHDP-1B
15
15.5
16
16.5
2
2
2
3
3
1
0 10 20
0 10 20
0 10 20
0 10 20
0 10
0 10
0
0
0 10
0
0 10 20 30
0 10
0 10
0
0 10 20
% of count

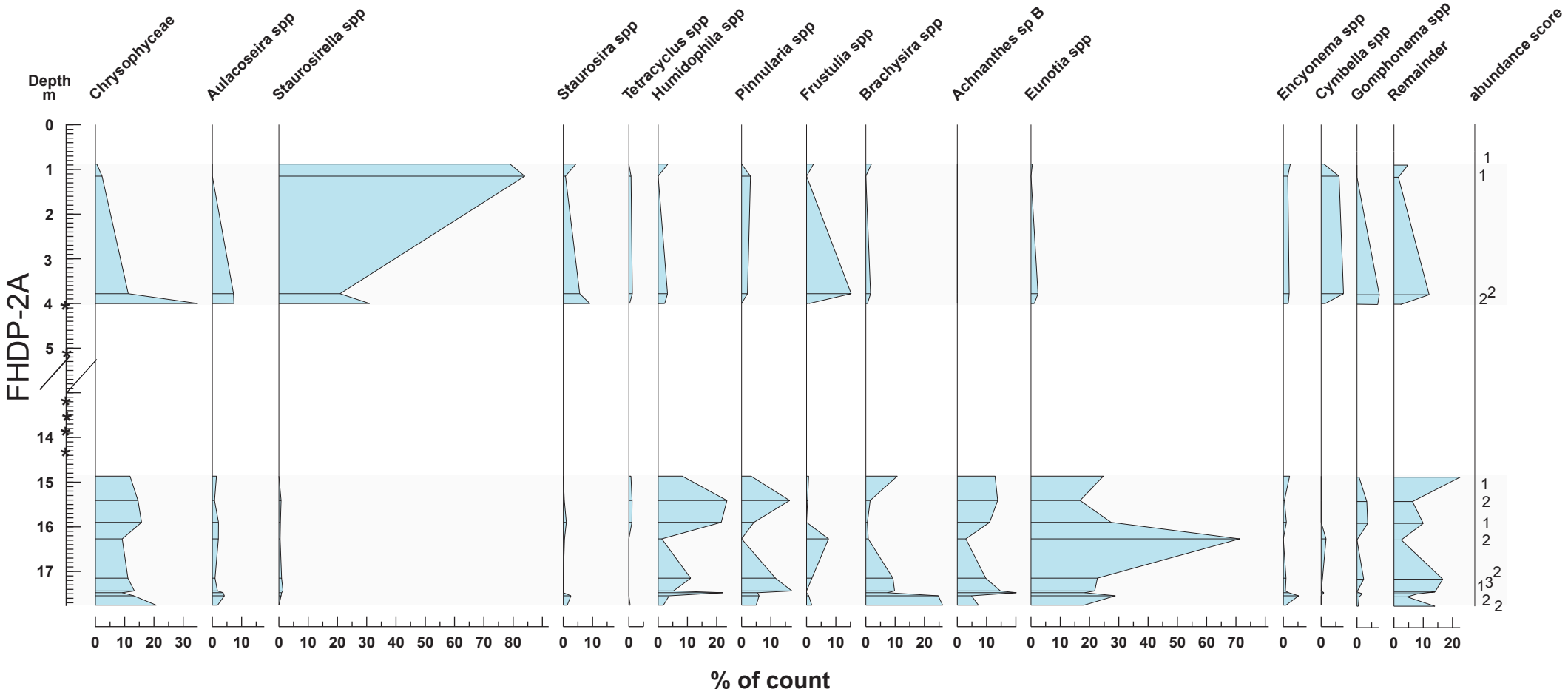
FHDP-2A
Depth m
Chrysophyceae
Aulacoseira spp
Staurosirella spp
Staurosira spp
Tetracyclus spp
Humidophila spp
Pinnularia spp
Frustulia spp
Brachysira spp
Achnanthes sp B
Eunotia spp
Encyonema spp
Cymbella spp
Gomphonema spp
Remainder
abundance score
% of count

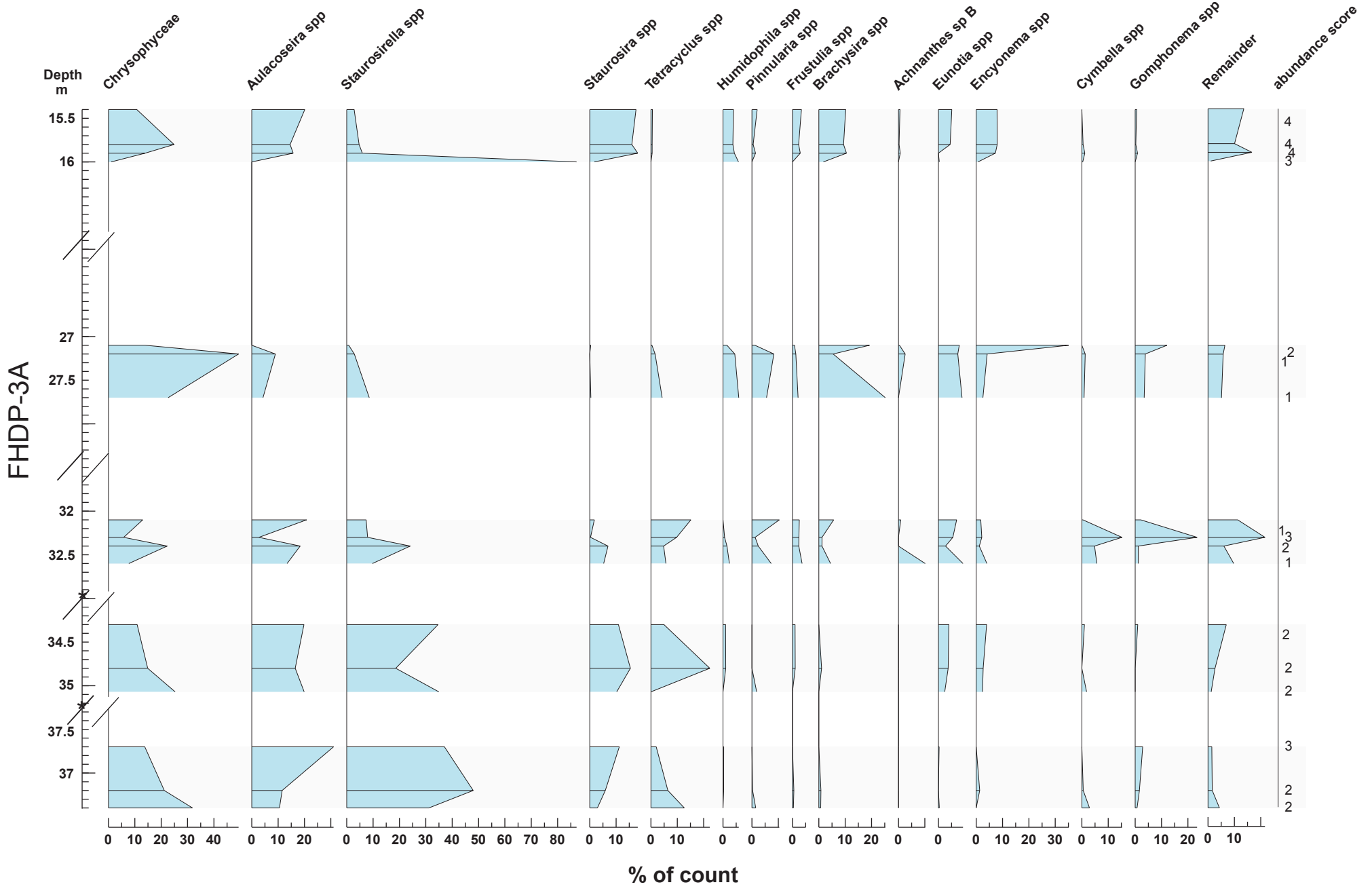
FHDP-3A
Depth m
Chrysophyceae
Aulacoseira spp
Staurosirella spp
Staurosira spp
Tetracyclus spp
Humidophila spp
Pinnularia spp
Frustulia spp
Brachysira spp
Achnanthes sp B
Eunotia spp
Encyonema spp
Cymbella spp
Gomphonema spp
Remainder
abundance score
15.5
16
27
27.5
32
32.5
34.5
35
37.5
37
% of count

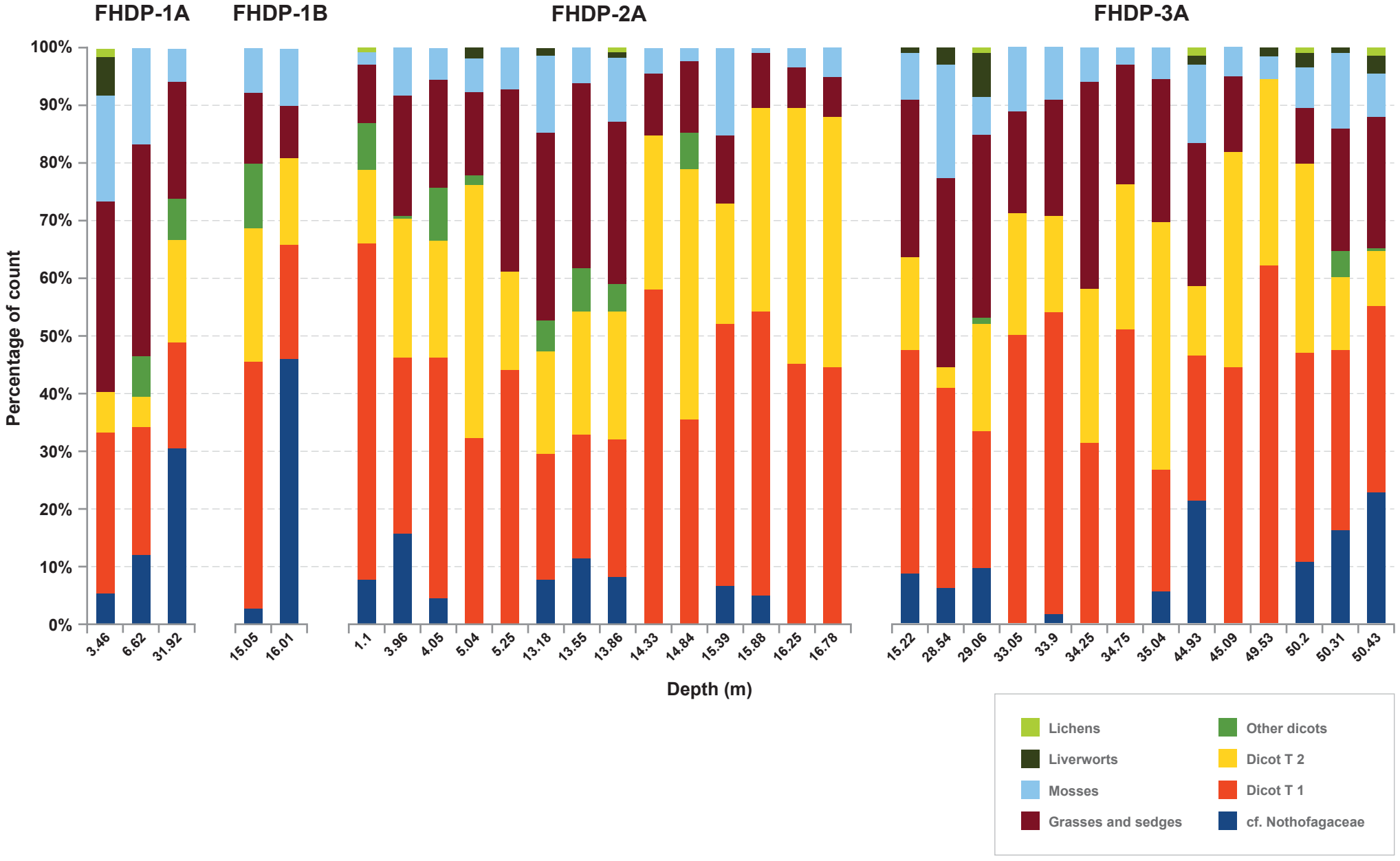
FHDP-1A
FHDP-1B
FHDP-2A
FHDP-3A
Percentage of count
100%
90%
80%
70%
60%
50%
40%
30%
20%
10%
0%
3.46
6.62
31.92
15.05
16.01
1.1
3.96
4.05
5.04
5.25
13.18
13.55
13.86
14.33
14.84
15.39
15.88
16.25
16.78
15.22
28.54
29.06
33.05
33.9
34.25
34.75
35.04
44.93
45.09
49.53
50.2
50.31
50.43
Depth (m)
Lichens
Liverworts
Mosses
Grasses and sedges
Other dicots
Dicot T 2
Dicot T 1
cf. Nothofagaceae

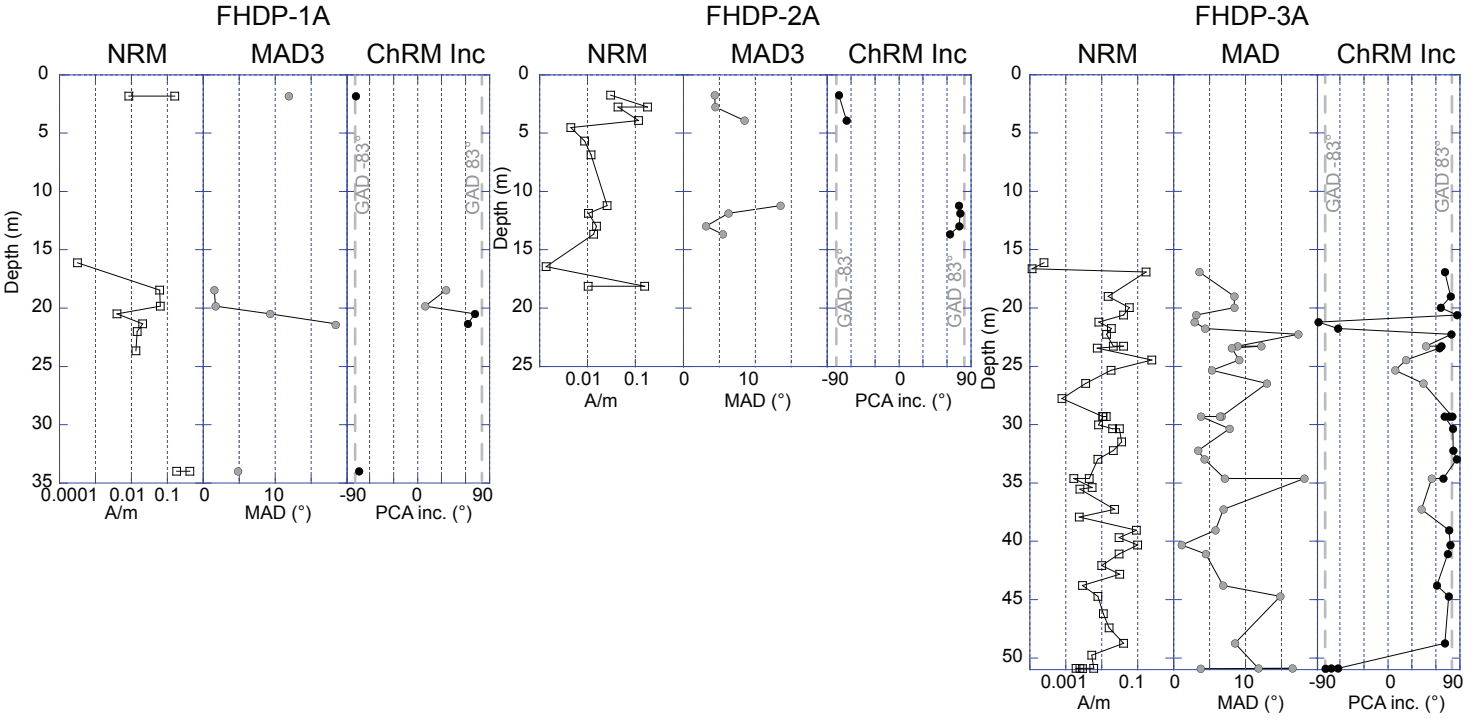
FHDP-1A
NRM
MAD3
ChRM Inc
Depth (m)
0
5
10
15
20
25
30
35
0.0001
0.01
0.1
A/m
0
10
MAD (°)
-90
0
90
PCA inc. (°)
GAD 83°
GAD 83°
FHDP-2A
NRM
MAD3
ChRM Inc
Depth (m)
0
5
10
15
20
25
0.01
0.1
A/m
0
10
MAD (°)
-90
0
90
PCA inc. (°)
GAD 83°
GAD 83°
FHDP-3A
NRM
MAD
ChRM Inc
Depth (m)
0
5
10
15
20
25
30
35
40
45
50
0.001
0.1
A/m
0
10
MAD (°)
-90
0
90
PCA inc. (°)
GAD 83°
GAD 83°

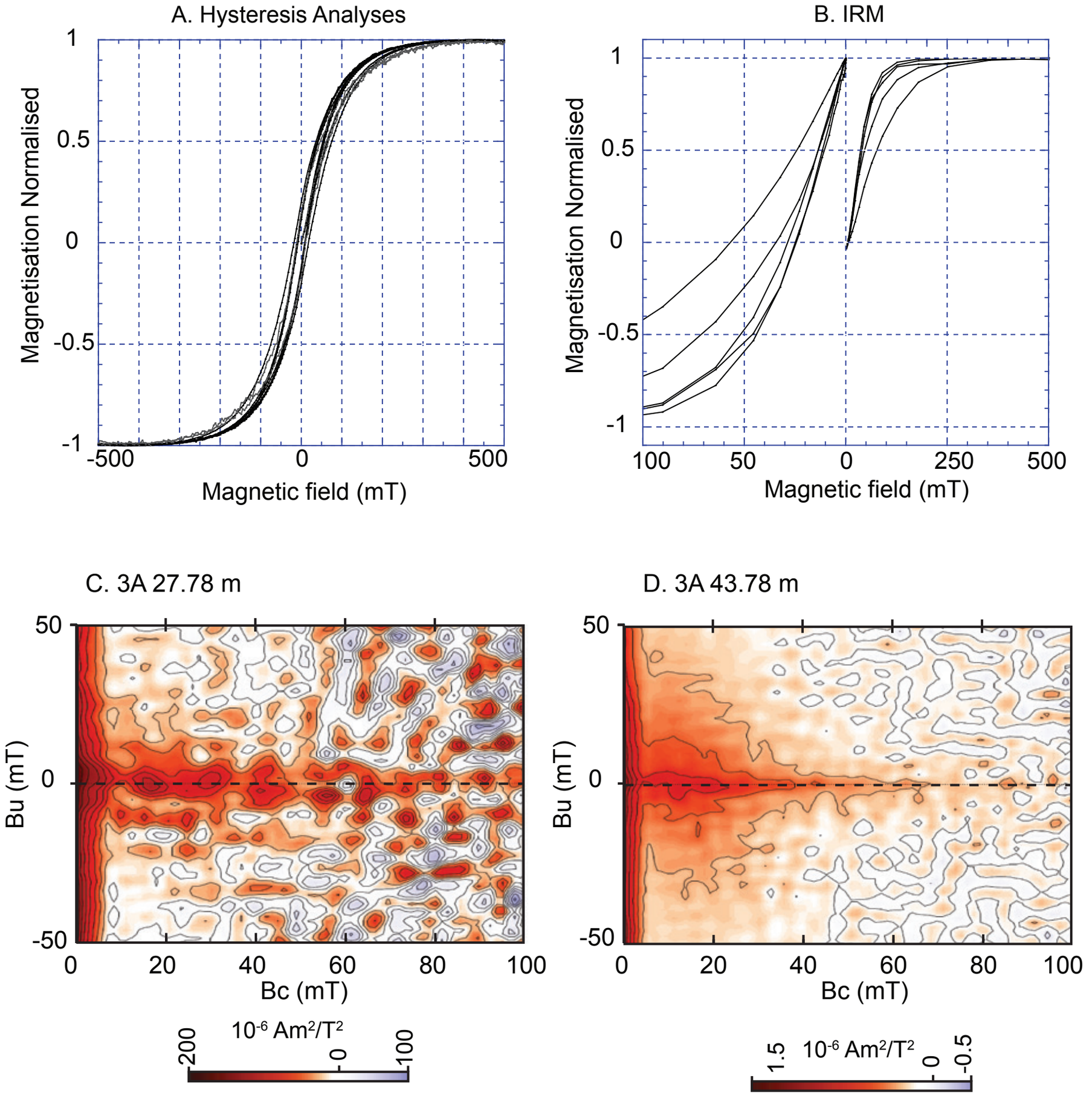
A. Hysteresis Analyses
Magnetisation Normalised
1
0.5
0
-0.5
-1
-500
0
500
Magnetic field (mT)
B. IRM
Magnetisation Normalised
1
0.5
0
-0.5
-1
100
50
0
250
500
Magnetic field (mT)
C. 3A 27.78 m
Bu (mT)
50
0
-50
0
20
40
60
80
100
Bc (mT)
10-6 Am2/T2
200
0
100
D. 3A 43.78 m
Bu (mT)
50
0
-50
0
20
40
60
80
100
Bc (mT)
10-6 Am2/T2
1.5
0
-0.5

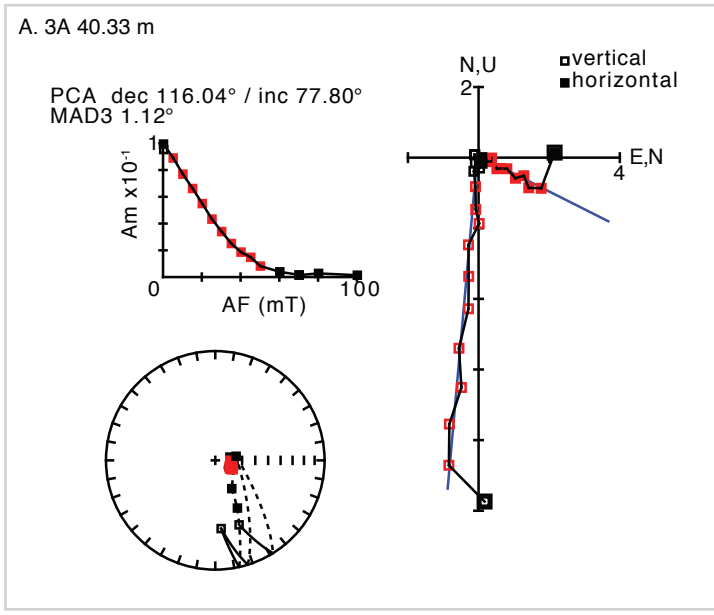
A. 3A 40.33 m
PCA dec 116.04° / inc 77.80°
MAD3 1.12°
Am x10⁻¹
AF (mT)
N,U
E,N
vertical
horizontal

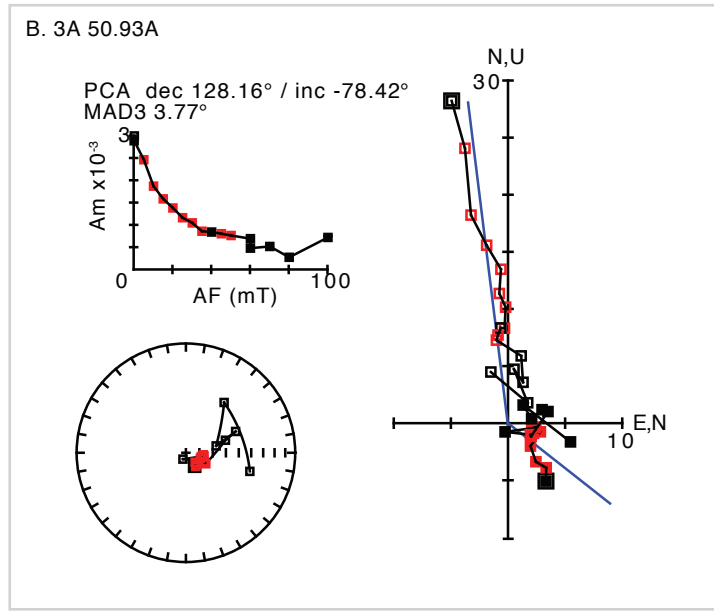
B. 3A 50.93A
PCA dec 128.16° / inc -78.42°
MAD3 3.77°
Am x10⁻³
AF (mT)
N,U
E,N

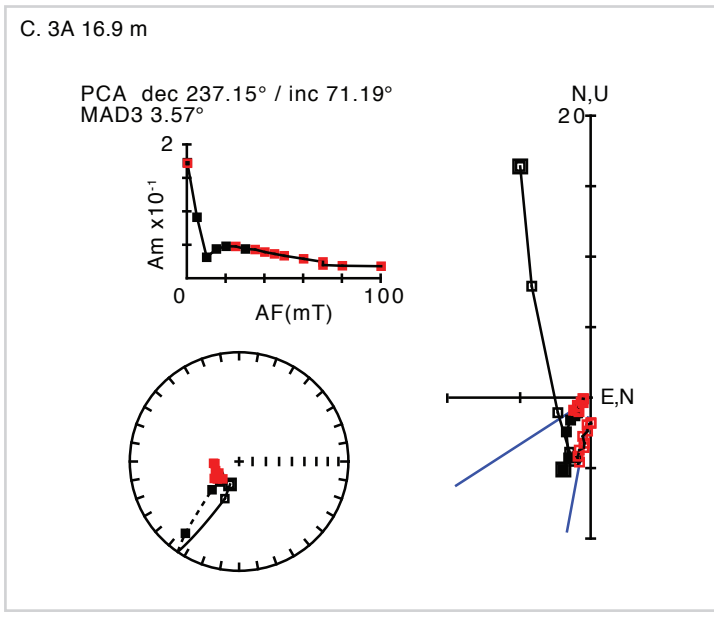
C. 3A 16.9 m
PCA dec 237.15° / inc 71.19°
MAD3 3.57°
Am x10⁻¹
AF(mT)
N,U
E,N

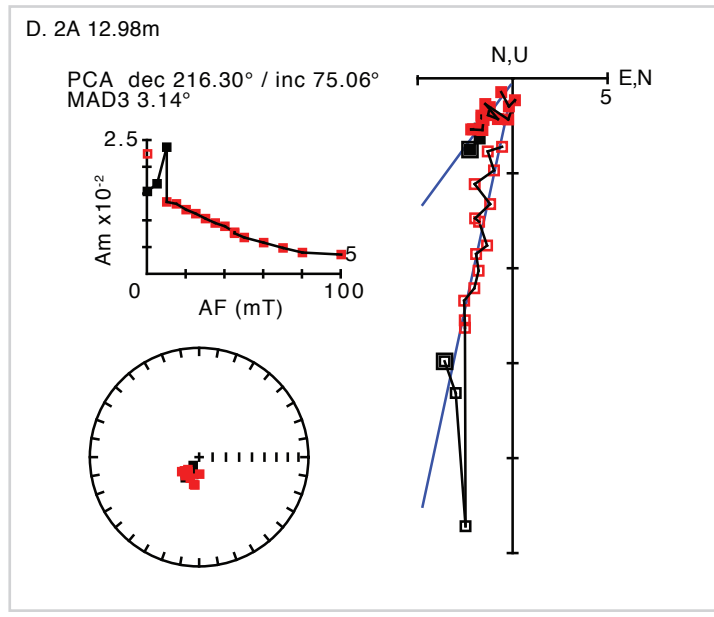
D. 2A 12.98m
PCA dec 216.30° / inc 75.06°
MAD3 3.14°
Am x10⁻²
AF (mT)
N,U
E,N

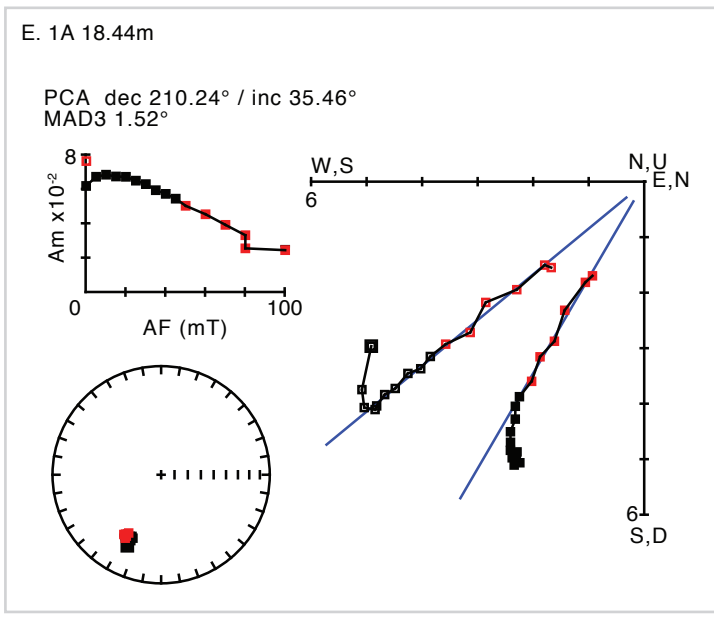
E. 1A 18.44m
PCA dec 210.24° / inc 35.46°
MAD3 1.52°
Am x10⁻²
AF (mT)
W,S
N,U
E,N
S,D

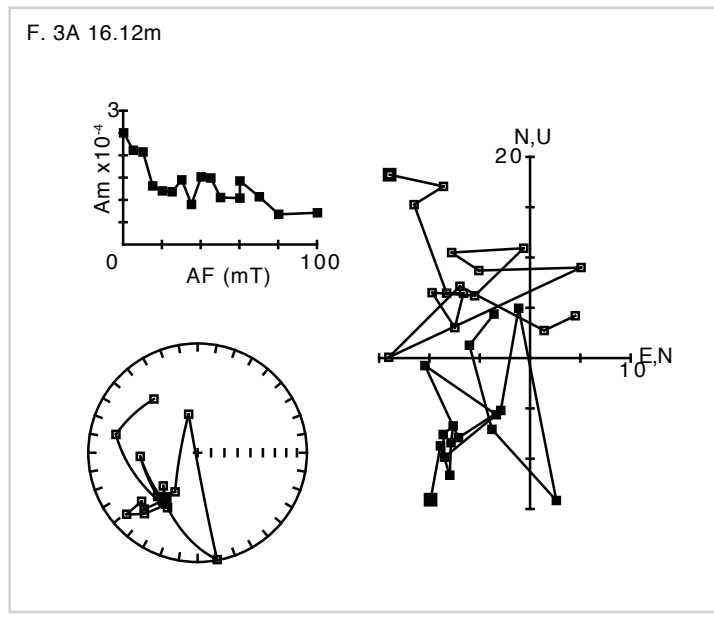
F. 3A 16.12m
Am x10⁻⁴
AF (mT)
N,U
E,N